



# Role of Grain Boundary Strength on Yielding Behavior and Uniaxial Tensile Properties in Ferritic Steels

Byeong-Seok Jeong<sup>1</sup> · Siwhan Lee<sup>1</sup> · Jeongwon Yeh<sup>1</sup> · Eun Soo Park<sup>1</sup> · Heung Nam Han<sup>1</sup>

Received: 21 February 2024 / Accepted: 10 June 2024  
© The Author(s) 2024

## Abstract

The yield-point phenomenon in recrystallized ferritic steels is often associated with the dislocation multiplication mechanism, wherein the yield drop can be attributed to the lack of mobile dislocations in materials. However, the yield-point phenomenon is not consistently observed in all recrystallized ferritic steels, implying that the dislocation multiplication mechanism has constraints in delineating the yielding behavior of these materials. Therefore, in this study, we introduced grain boundary strength as a critical parameter for elucidating the yielding behavior of recrystallized ferritic steels. Three types of steels—interstitial-free (IF) steel, precipitation-hardened (PH) steel, and Mn-added interstitial-free (IF-2Mn) steel—were analyzed for grain boundary strength using nanoindentation, and the reliability of this methodology was verified by Hall–Petch analysis. The IF steel, which lacked the yield-point phenomenon, demonstrated a much lower grain boundary strength than the PH and IF-2Mn steels, where the phenomenon occurred. Microstructural analysis confirmed that the enhanced grain boundary strengths of the PH and IF-2Mn steels were due to carbon and manganese segregation at the grain boundaries, respectively. Further, the grain boundary strength significantly influenced the tensile properties and yielding behavior. In PH steels, the enhanced grain boundary strength increased the yield strength owing to Hall–Petch hardening; however, it also increased the resistance to plastic deformation propagation, resulting in reduced ductility. In the IF-2Mn steels, the two specimens with different grain sizes exhibited similar yield strengths, which could be attributed to differences in the grain boundary strength. Our findings have significant implications for the design and optimization of ferritic steels.

**Keywords** Grain boundary strength · Yield-point phenomenon · Uniaxial tensile properties · Ferritic steel

## 1 Introduction

In polycrystalline materials, grain boundaries act as barriers to the propagation of plastic deformation by impeding dislocation movements [1–7]. During the initial microyielding stage, the interactions between the mobile dislocations within the grains and the grain boundaries result in a dislocation pile-up at the grain boundaries. Dislocations in a pile-up exert shear stress, known as pile-up stress, to the grain boundaries, induced by the overlap of Peach–Koehler forces [8, 9].

With the increase in the number of dislocations in a pile-up, the pile-up stress gradually intensifies, reaching

the critical activation stress, known as the grain boundary strength. At this point, dislocations are emitted from the grain boundaries, which initiate the propagation of plastic deformation to neighboring grains, leading to the onset of macro-yielding [10–15].

As the grain boundary strength indicates how effectively the grain boundaries impede dislocation movement during the initial yield stage, the grain boundary strength is closely related to the Hall–Petch coefficient. The relationship between the grain boundary strength and Hall–Petch coefficient can be expressed as follows:

$$k_y = M \left( \frac{Gb\tau^*}{k\pi} \right)^{1/2} \quad (1)$$

where  $k_y$  is the Hall–Petch coefficient,  $M$  is the Taylor factor,  $G$  is shear modulus,  $b$  is the burgers vector,  $k$  is a constant that is dependent on the character of the dislocation, and  $\tau^*$  is the grain boundary strength [16–21]. This equation suggests that with an increase in  $\tau^*$ , the Hall–Petch coefficient

✉ Heung Nam Han  
hnhan@snu.ac.kr

<sup>1</sup> Department of Materials Science and Engineering and Research Institute of Advanced Materials, Seoul National University, Seoul 08826, Republic of Korea

correspondingly increases. Consequently, an enhanced contribution of the Hall–Petch hardening to the yield strength can be anticipated even without reducing the grain size, as indicated by the Hall–Petch equation:

$$\sigma_y = \sigma_0 + k_y d^{-1/2} \quad (2)$$

where  $\sigma_y$  is the yield stress,  $\sigma_0$  is the friction stress,  $k_y$  is the Hall–Petch coefficient, and  $d$  is the average grain size [16, 17, 22].

The Hall–Petch coefficient is influenced by the microstructural characteristics of the grain boundaries. Numerous studies have reported an increase in the Hall–Petch coefficient with increasing grain boundary segregation of solute atoms in ferritic steels [18, 23–26]. This implies that the grain boundary segregation of solute atoms makes it increasingly challenging for the emission of dislocations from the grain boundary. In addition, the Hall–Petch coefficient is closely related to the yielding behavior of the material. Gao et al. reported that high-purity iron exhibiting discontinuous yielding behavior has a higher Hall–Petch coefficient than that with continuous yielding behavior [27]. Considering that the Hall–Petch coefficient is determined by  $\tau^*$ , according to Eq. (2), the yielding behavior of the material may be closely related to  $\tau^*$ .

The yielding behavior of most metals and alloys is characterized by a gradual transition from elastic to plastic deformation, known as continuous yielding. However, in certain cases, the yielding behavior exhibits an abrupt transition, with a conspicuous yield drop, followed by a plateau, known as discontinuous yielding.

The discontinuous yielding behavior of steels has been explained using microstructural approaches such as the Cottrell–Bilby theory [28–31] and dislocation multiplication mechanisms [32–36]. The Cottrell–Bilby theory is particularly convincing for materials with a high density of mobile dislocations along with a sufficient number of pinning particles, such as solute atoms or precipitates.

However, in the case of materials with extremely low mobile dislocation densities owing to recrystallization, the occurrence of the yield-point phenomenon is often associated with the initiation of dislocation multiplication. Nonetheless, it is essential to recognize that the yield-point phenomenon does not consistently occur just because dislocation multiplication occurs during the initial yielding.

Even in recrystallized microstructures, variations in grain size and chemical composition can render varied yielding behaviors. Tian et al. reported that the yielding behavior of fully recrystallized copper varies depending on the grain size [37]. The yield-point phenomenon was observed only when the grain size ranged from 0.5 to 3  $\mu\text{m}$ , while continuous yielding behavior was observed at other grain size intervals. Gao et al. reported variations in yielding behavior

with grain size in recrystallized interstitial-free steel [38]. As the grain size decreased, the yielding behavior shifted from continuous to discontinuous, leading to a yield drop. Moreover, recent studies have shown that varying chemical compositions can affect yielding behavior, even when grain sizes are similar [18, 23, 24].

Thus, the yielding behavior of recrystallized steel can vary depending on microstructural factors, even when the initial yield is initiated by dislocation multiplication. Therefore, it is necessary to examine the microstructural mechanism that can explain the volatile yielding behavior of recrystallized steel.

The microstructural mechanism of the yielding behavior associated with  $\tau^*$  is schematically shown in Fig. 1 [12]. According to this mechanism, the yielding behavior of polycrystalline materials is determined by the interplay between  $\tau^*$  and  $\tau_p$ . With the initiation and progression of deformation, dislocations tend to accumulate at the grain boundaries, a phenomenon known as dislocation pile-up. The piled-up dislocations exert repulsive forces on each other, ultimately exerting shear stress, known as pile-up stress, at the grain boundaries, as indicated by ① in Fig. 1a, b. If the density of the pile-up dislocations is sufficient for  $\tau_p$  to reach  $\tau^*$  at yielding, as indicated by ② in Fig. 1a, the material displays continuous yielding behavior. Conversely, if  $\tau_p$  does not reach  $\tau^*$  just before yielding, as shown by ② in Fig. 1b, external stress is required for  $\tau_p$  to reach  $\tau^*$  at the initial yielding, resulting in the upper yield point. Upon yielding, concurrent with dislocation multiplication in adjacent grains, the number of dislocations available for pile-up increases, as shown by ③ in Fig. 1b. This leads to  $\tau_p$  reaching  $\tau^*$  with either reduced or no external stress assistance in adjacent grains, ultimately causing a load drop and the lower yield point.

In summary,  $\tau^*$  is a decisive parameter for the yielding behavior of a material. Therefore, this study focuses on  $\tau^*$  in understanding the yielding behavior of recrystallized ferritic steels. Initially, we introduce a method to measure  $\tau^*$  using nano-indentation and verify its reliability through Hall–Petch analysis. Utilizing this method, we analyze  $\tau^*$  for recrystallized ferritic steel specimens and discuss the effect of  $\tau^*$  on the yielding behavior and uniaxial tensile properties. Furthermore, the microstructural factors that contribute to the differences in  $\tau^*$  among the specimens examined were analyzed. Based on these results, the microstructural mechanisms that govern the yielding behavior and uniaxial tensile properties of recrystallized ferritic steels were elucidated.

## 2 Materials and Methods

Three ferritic steels with different chemical compositions were used: interstitial-free (IF), precipitation-hardened (PH), and Mn-added interstitial-free (IF-2Mn). The detailed

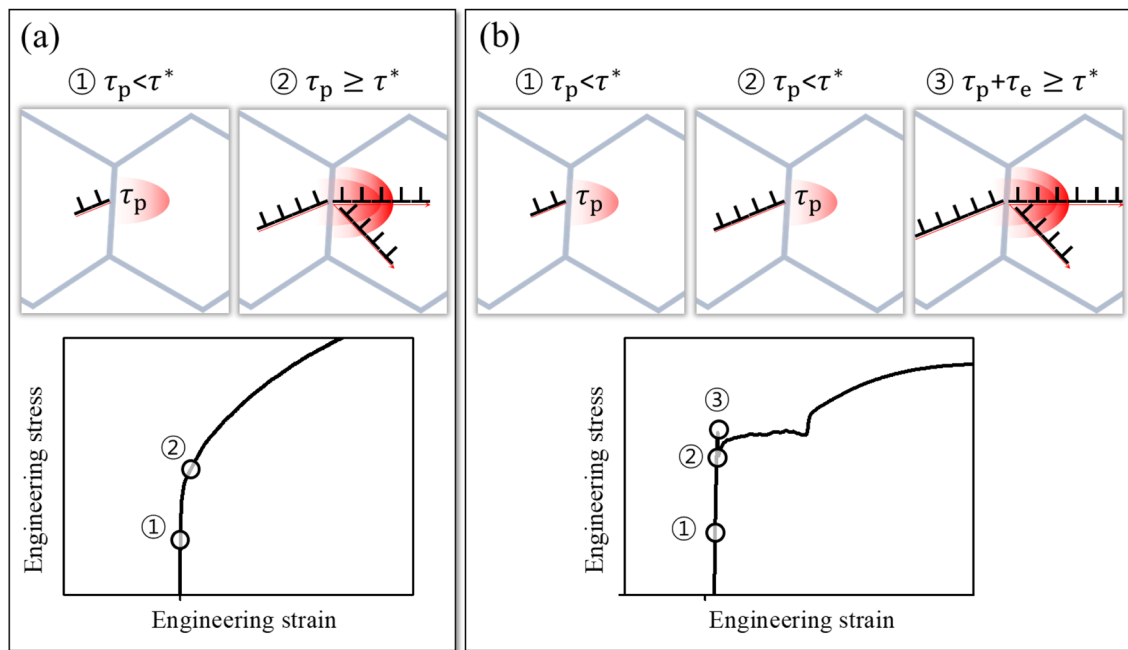


**Fig. 1** Schematic illustration of the relationship between pile-up stress and grain boundary strength related to **a** continuous yielding behavior and **b** discontinuous yielding behavior

chemical compositions are listed in Table 1. In IF and IF-2Mn steels, a sufficient amount of titanium was added to fix carbon as titanium carbide, preventing carbon segregation at the grain boundaries. In the PH steel, titanium was intentionally excluded to maintain the carbon as an interstitial atom, thereby promoting its segregation at the grain boundary. In IF-2Mn steel, manganese, a substitutional solute prone to segregation at the grain boundaries, was added. The as-received IF (IF-AS) and PH (PH-AS) steels were hot rolled to a thickness of 2 mm. The as-received IF-2Mn steel was fabricated using high-purity arc-melting elements, followed by drop casting using a water-cooled copper mold to obtain a plate-type specimen with dimensions of  $4 \times 12 \times 40 \text{ mm}^3$ . Each specimen underwent specific heat treatments and a cold rolling process for various purposes. IF steel aimed to achieve different average grain sizes, PH steel aimed to induce differences in solute atom distribution near grain boundaries, and IF-2Mn steel aimed for both objectives. IF-AS was cold-rolled to a thickness of 1.2 mm, then heated at a rate of  $10 \text{ }^\circ\text{C per min}$ , and held at  $700 \text{ }^\circ\text{C}$  for 5, 30, and 7200 min, or at  $800 \text{ }^\circ\text{C}$  for 7200 min, before being air-cooled. PH-AS was heated to  $200 \text{ }^\circ\text{C}$  (PH-200) and  $600 \text{ }^\circ\text{C}$

(PH-600) with a heating rate of  $10 \text{ }^\circ\text{C per min}$ , held for 20 h, followed by air cooling. IF-2Mn-AS was cold-rolled to a thickness of 1.2 mm, then heated at a rate of  $10 \text{ }^\circ\text{C per min}$  to  $800 \text{ }^\circ\text{C}$ , with IF-2Mn-1 held for 15 min and IF-2Mn-2 for 150 min before air cooling.

Uniaxial tensile tests were performed using a tensile testing machine (5582, INSTRON) at a strain rate of  $10^{-3} \text{ s}^{-1}$  under displacement-controlled conditions at room temperature ( $25 \text{ }^\circ\text{C}$ ). Tensile specimens were prepared according to the ASTM E8 sub-size standard. A clip-on extensometer was attached to the tensile specimen during the tensile test to measure the tensile strain. Herein, the yield strength of the specimens is defined as the upper yield stress when the specimen exhibits discontinuous yielding, and 0.2% offset yield stress when the specimen shows continuous yielding.

The samples for the microstructure characterization were polished by a standard mechanical grinding and polishing procedure, followed by electropolishing in a solution of 10% perchloric acid and 90% ethanol at 25 V for 30 s. The etchant for revealing the grain boundaries was a 2% nital solution. A field-emission scanning electron microscope (GeminiSEM 560, ZEISS) equipped with an electron backscatter

**Table 1** Chemical compositions of ferritic steels used in this study (wt%)

	C	Mn	Ti	Nb	Si	Fe
IF	0.002	0.09	0.02	0.015	–	Bal
PH	0.08	0.9	–	0.03	0.2	Bal
IF-2Mn	–	2.0	0.02	–	–	Bal

diffraction (EBSD) detector (HKL Channel 5, Oxford) and an energy dispersive X-ray spectroscopy (EDS) detector was used, and post-processing was conducted using TSL OIM Analysis 7 software. From the post-processed EBSD data, the inverse pole figure (IPF) and grain orientation spread (GOS), which quantify the average misorientation angles to the grain mean orientation, were visualized as maps. Electron probe microanalysis (EPMA) was conducted using a field-emission scanning electron microscope (JXA-8530F, JEOL) equipped with wavelength-dispersive spectrometer (WDS) detectors operated at 15 kV and a probe current of 400 nA.

A nanoindentation test (Ti 750L Ubi, Hysitron) was conducted to analyze the dislocation behavior related to the initial yielding and nano-hardness at room temperature (25 °C). The specimens for the nanoindentation test were prepared identically to those used for the microstructure characterization. Nanoindentation tests were conducted in a load control mode with constant loading and unloading rates of  $200 \mu\text{N s}^{-1}$ . The maximum load was set at  $1000 \mu\text{N}$  for both the IF and PH samples and  $5000 \mu\text{N}$  for the IF-2Mn sample. A 2-s hold period was implemented at the maximum load for all samples. A diamond Berkovich indenter tip was used, and the area function of the tip was calibrated using standard fused quartz, according to the method outlined by Pharr and Oliver [39]. A total of 100 indentations ( $10 \times 10$

with an interval of  $40 \mu\text{m}$ ) were made on each specimen; thereafter, SEM was used to distinguish indentation data performed at grain boundaries.

### 3 Results and Discussion

#### 3.1 Yielding Behavior of Recrystallized Ferritic Steels

The microstructures of the IF-AS and PH-AS specimens observed using EBSD are shown in Fig. 2. The IPF maps (Fig. 2a, c) show that the microstructures of both specimens consist of polygonal ferrite. Under a critical misorientation angle for grain boundaries at  $15^\circ$ , the average grain size of the two specimens was  $25.9$  and  $10.1 \mu\text{m}$ , respectively. The GOS maps (Fig. 2b, d) show that most grains in both specimens have GOS values of less than  $2^\circ$ , indicating that the specimens have a recrystallized microstructure. Figure 3 shows the uniaxial tensile test results for IF-AS and PH-AS, with IF-AS displaying continuous yielding behavior, and PH-AS displaying discontinuous yielding with a clear yield-point phenomenon. Recrystallized materials are expected to undergo dislocation multiplication during the initial yielding stage, potentially leading to the yield-point phenomenon [32,

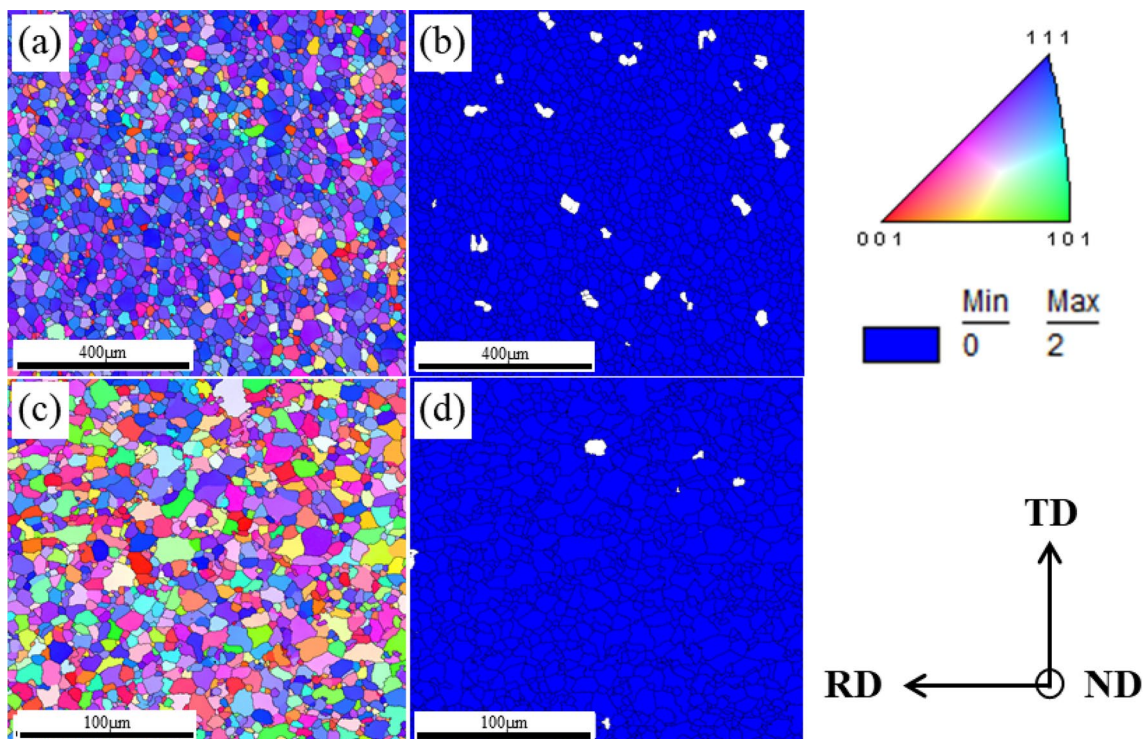


**Fig. 2** The EBSD maps of **a, b** IF-AS and **c, d** PH-AS: **a, c** Inverse pole figure (IPF) ND map and **b, d** Grain orientation spread (GOS) map. Grains with GOS value smaller than  $2^\circ$  and grains with GOS value larger than  $2^\circ$  are marked in blue and white, respectively in **b, d**

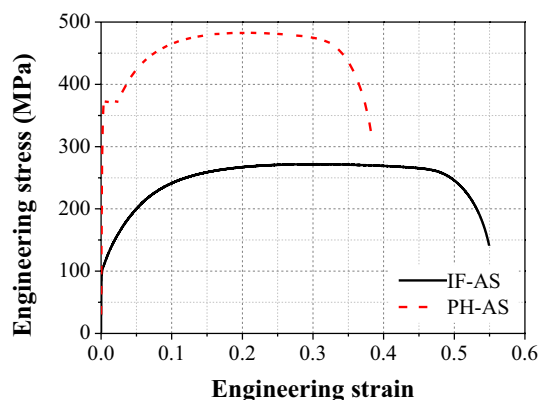


**Fig. 3** Engineering stress–strain curve of **a** IF-AS and **b** PH-AS during uniaxial tensile test at 25 °C of room temperature for the strain rate  $10^{-3} \text{ s}^{-1}$

33]. In PH-AS, a recrystallized material, a yield-point phenomenon was observed. However, in IF-AS, which is also a recrystallized material, although dislocation multiplication had to occur during the initial yielding stage, a continuous yielding behavior was observed. This implies the occurrence of dislocation multiplication during the initial yielding stage does not guarantee the presence of the yield-point phenomenon. Thus, the microstructural factors that determine the presence or absence of the yield-point phenomenon in recrystallized materials have not been established. In this study,  $\tau^*$  is introduced as a microstructural factor that determines the yielding behavior of recrystallized materials.

### 3.2 Evaluation of Grain Boundary Strength Using Nanoindentation Test

We performed nanoindentation tests on the grain boundaries to evaluate  $\tau^*$ . Figure 4 shows the load–displacement curve of the IF-AS specimen obtained via nanoindentation tests at the grain boundaries. The dashed lines in Fig. 4a, which fit closely in the initial stages of the profiles, are the theoretical Hertzian elastic contact solutions, assuming that the indenter tip is spherical at shallow depths, as expressed in Eq. (3):

$$P = \frac{4}{3} E_r \sqrt{Rh^3} \quad (3)$$

where  $P$ ,  $h$ ,  $E_r$ , and  $R$  denote the load applied using a spherical indenter tip, the corresponding indentation depth, the reduced elastic modulus of approximately 192 GPa, and the effective radius of the indenter tip of approximately 430 nm, respectively [39, 40]. The indenter tip undergoes an instantaneous jump in the depth direction without additional loading where the profile deviates from the Hertzian solution; this is termed a pop-in phenomenon, which is usually interpreted as a trace of dislocation nucleation or dislocation source activation associated with the onset of plastic yielding [41–47]. Therefore, the pop-in load obtained via nanoindentation tests at the grain boundaries can be converted to the maximum shear stress ( $\tau_{\max}$ ) required for dislocation nucleation at the grain boundaries, representing  $\tau^*$ , using Eq. (4):

$$\tau_{\max} = 0.31 \left( \frac{6P_p E_r^2}{\pi^3 R^2} \right) \quad (4)$$

where  $P_p$  denotes the pop-in load [40]. Figure 4b shows the cumulative probability for  $\tau_{\max}$  of IF-AS obtained using Eq. (4). The  $\tau_{\max}$  value of IF-AS was in the range

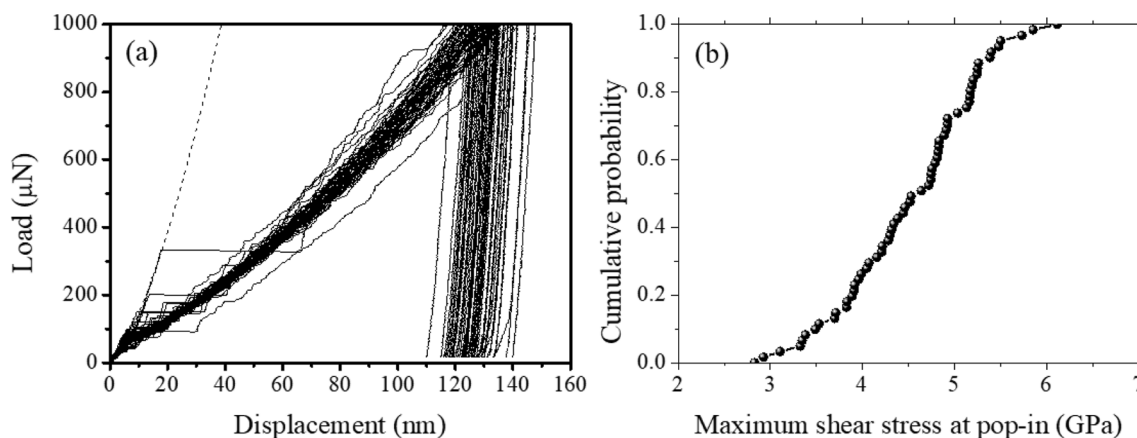


**Fig. 4** **a** Load–displacement curve obtained during nano-indentation tests at grain boundary of IF-AS. **b** Cumulative probability of maximum shear stress at pop-in for IF-AS

of 2.8–6.1 GPa, corresponding to  $G/28$ – $G/13$ , where  $G$ , the shear modulus of the steel, is 77 GPa. Considering that these values are within the range of the theoretical strength ( $G/30$ – $G/6$ ) of a crystalline material [48], the pop-in at the grain boundaries of IF-AS is a result of dislocation nucleation. These results confirm that  $\tau_{\max}$  refers to  $\tau^*$ , which is the shear stress required for dislocation nucleation at the grain boundaries.

To ensure the reliability of measuring  $\tau^*$  using nanoindentation, in addition to comparing  $\tau_{\max}$  with the theoretical strength mentioned above, a Hall–Petch analysis was conducted. We compared the value of  $k_y$  obtained using the conventional method for analyzing the grain-size dependence of yield strength with that calculated by substituting  $\tau_{\max}$  into  $\tau^*$  in Eq. (1). This comparison aimed to determine whether  $\tau^*$  can be estimated using  $\tau_{\max}$ . For conventional Hall–Petch analysis, IF-AS specimens with grains of various sizes were prepared by heat treatment at various temperatures and times. Figure 5 shows the microstructures of the IF specimens with different grain sizes observed through SEM/EBSD. The grain size ranged from 25.9 to 118  $\mu\text{m}$ . In the GOS maps shown in Fig. 5b, d, f, h, j, it can be observed that most grains have a recrystallized microstructure with a GOS value of less than  $2^\circ$ . Figure 6a shows the engineering stress–strain curve for each specimen during the uniaxial

tensile test. According to the Hall–Petch relationship, the yield strength decreases as the grain size increases. The yield strength was plotted against the inverse square root of the grain size in Fig. 6b, and the value of  $k_y$  obtained by fitting Eq. (2) was  $369.6 \text{ MPa}\cdot\mu\text{m}^{-1/2}$ . Furthermore, the value of  $k_y$  calculated using an average  $\tau_{\max}$  of 4.51 GPa and Eq. (1) with parameters  $M$ ,  $G$ ,  $b$ ,  $k$  set to 2, 77 GPa, 2.48 Å, 0.85, respectively [49], was  $362 \text{ MPa}\cdot\mu\text{m}^{-1/2}$ . It was confirmed that the two  $k_y$  values obtained using the different methods exhibited similarity. This result implies that the methodology for estimating  $\tau^*$  using the nanoindentation test at the grain boundary is reliable.

### 3.3 Grain Boundary Strengthening by Carbon Segregation

Based on the methodology described above, we compared the  $\tau^*$  values of IF and PH specimens with different yielding behaviors and mechanical properties. Based on the results, we analyzed the influence of  $\tau^*$  on the mechanical behavior of the IF and PH specimens.

Figure 7 shows the microstructures of PH-200 and PH-600 observed using SEM/EBSD. The IPF maps in Fig. 7a, c show that the microstructure is composed of equiaxed grains with an almost random texture. The GOS

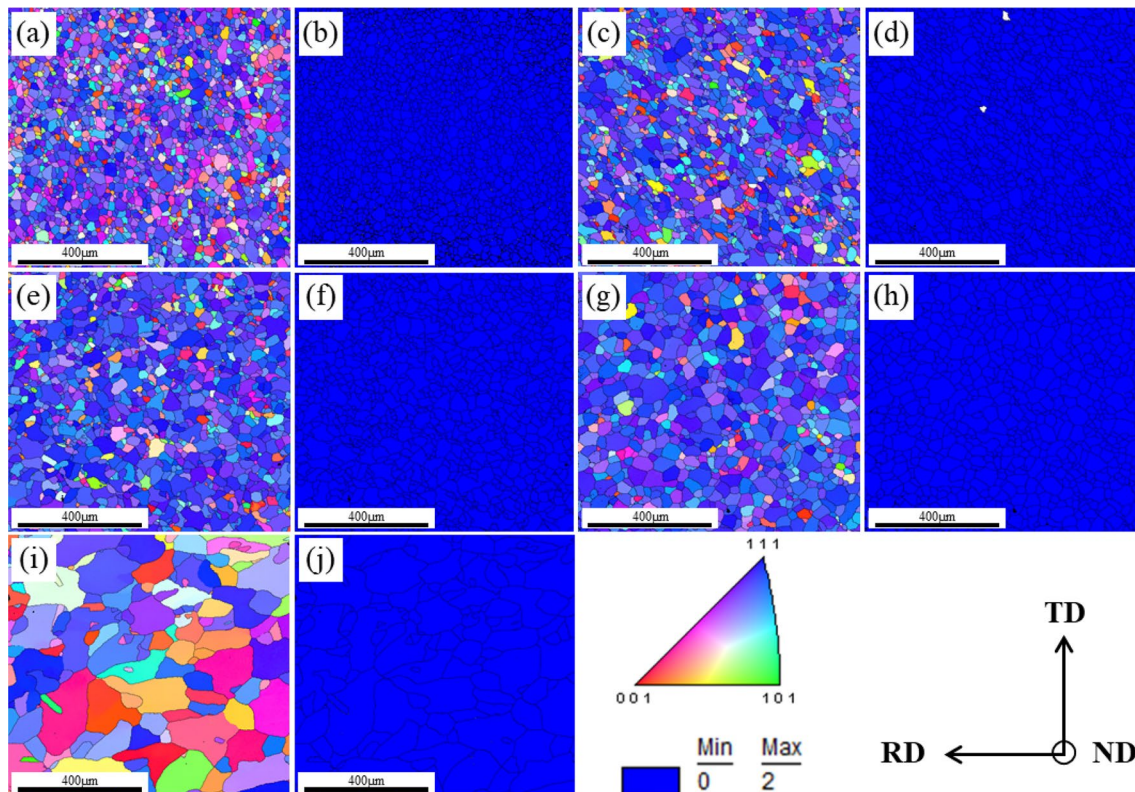


**Fig. 5** The EBSD maps of heat-treated IF-AS specimens with an average grain size of **a**, **b** 25.9  $\mu\text{m}$ , **c**, **d** 33.4  $\mu\text{m}$ , **e**, **f** 38.3  $\mu\text{m}$ , **g**, **h** 42.7  $\mu\text{m}$  and **i**, **j** 118  $\mu\text{m}$ . **a**, **c**, **e**, **g**, **i** IPF ND map and **b**, **d**, **f**, **h**, **j** GOS map

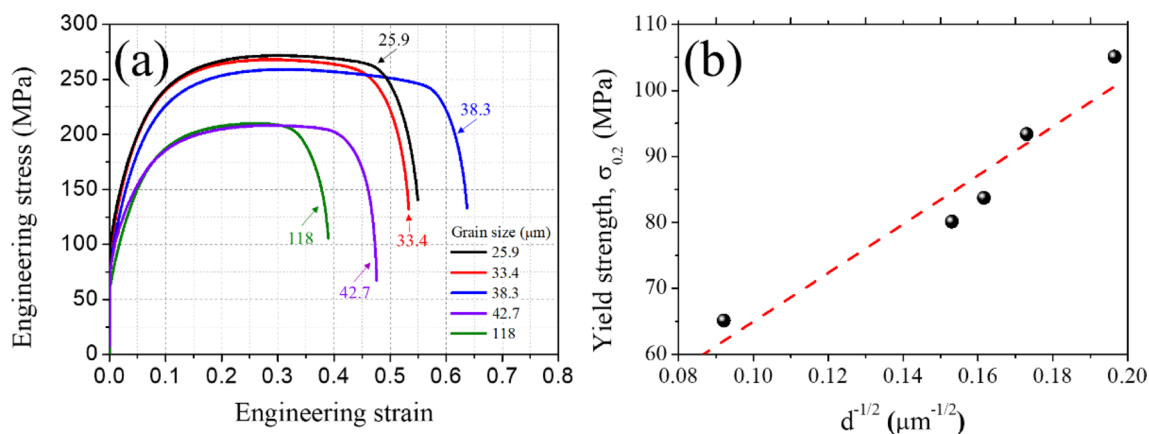


**Fig. 6** **a** Engineering stress–strain curve of IF-AS specimens with a various grain size during uniaxial tensile test at 25 °C of room temperature for the strain rate  $10^{-3} \text{ s}^{-1}$ . **b** Variation of yield strength with

inverse root square of grain size for IF-AS. The data has been fitted with a Hall–Petch equation (dashed red line)

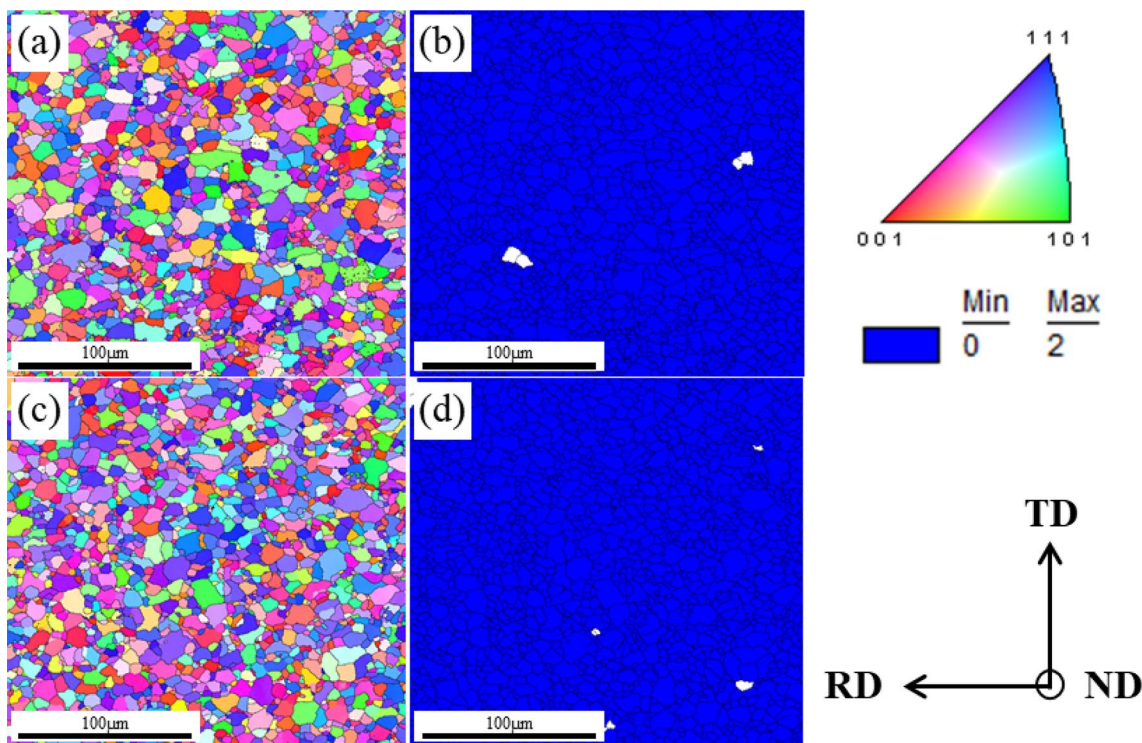


**Fig. 7** The EBSD maps of **a, b** PH-200 and **c, d** PH-600. **a, c** IPF ND map and **b, d** GOS map

maps in Fig. 7b, d show that most grains have GOS values of  $2^\circ$  or less, indicating that the specimen has a recrystallized structure. The grain sizes of PH-200 and PH-600 were 9.36 and 9.05  $\mu\text{m}$ , respectively, similar to those of PH-AS. Figure 8 shows the uniaxial tensile test results for the PH specimens. All the PH specimens exhibited discontinuous yielding behavior. However, the uniaxial tensile properties of each specimen were different, even though there was little microstructural difference between the specimens in the

SEM/EBSD analysis, as shown in Figs. 3 and 7. Table 2 presents the uniaxial tensile properties of the PH specimens. In the case of PH-200, the yield strength increased, the tensile strength remained similar, and the total elongation decreased compared with that of PH-AS. In PH-600, the yield strength increased, whereas both the tensile strength and total elongation decreased compared to those in PH-AS. The reason for the variation in the mechanical properties based on the heat treatment history can be inferred from the results of the

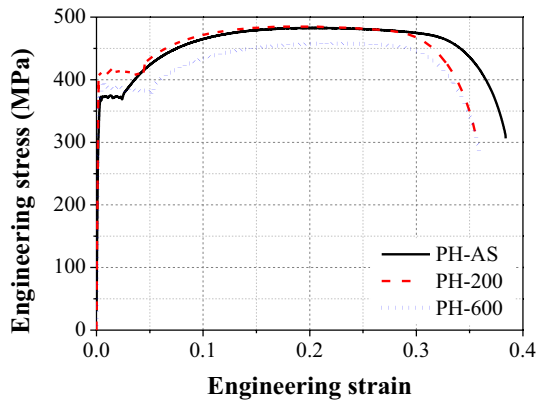


**Fig. 8** Engineering stress–strain curve of PH specimens during uniaxial tensile test at 25 °C of room temperature for the strain rate  $10^{-3} \text{ s}^{-1}$

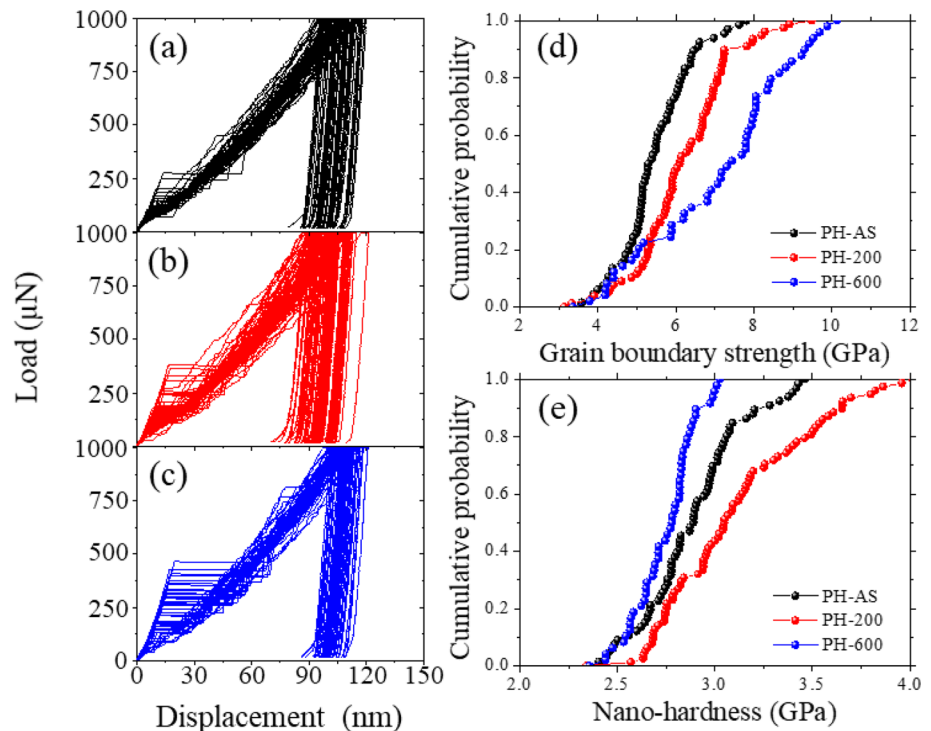
**Table 2** Uniaxial tensile properties of PH specimens

	Yield strength (MPa)	Tensile strength (MPa)	Total elongation (%)
PH-AS	373	483	38
PH-200	410	485	36
PH-600	398	457	36

nanindentation test at the grain boundary shown in Fig. 9 and the phase diagram obtained from the FactSage program shown in Fig. 10.

The load–displacement curves of PH-AS (black), PH-200 (red), and PH-600 (blue) are presented in Fig. 9a–c. The cumulative probability of  $\tau^*$  and the nano-hardness values obtained from Fig. 9a–c are presented in Fig. 9d, e. As shown in Fig. 9d, the distribution of  $\tau^*$  shifts to higher values in the order of PH-AS, PH-200, and PH-600. Equation (1) shows that an increase in  $\tau^*$  leads to an increase in the Hall–Petch coefficient. With a higher Hall–Petch coefficient, the material undergoes increased Hall–Petch hardening without altering the grain size, resulting in a higher yield strength. Therefore, despite similar grain sizes, the yield strengths of PH-200 and PH-600 appeared to be higher than that of PH-AS, as displayed in Table 2. This result implies that  $\tau^*$  is closely related to the yielding behavior of the material. Furthermore, the increase in  $\tau^*$  for PH-200 and PH-600 implies an enhanced resistance of the grain boundaries to the propagation of plastic deformation, which appears to reduce the total elongation of both specimens. Although PH-600 had the highest  $\tau^*$ , the yield strength was the highest for PH-200, which can be inferred from the phase diagram of the PH specimen shown in Fig. 10. According to the phase diagram,  $\text{M}_7\text{C}_3$  carbide exists at 200 °C but dissolves at 600 °C in the equilibrium state. Based on this result, it can be inferred that the dissolution of carbides led to a reduction in the precipitation hardening in PH-600. Therefore, although the Hall–Petch hardening was greater in PH-600 than in PH-200, the precipitation hardening decreased because of

**Fig. 9** Load–displacement curve of a PH-AS, b PH-200 and c PH-600. Cumulative probability of d grain boundary strength and e nano-hardness for PH specimens





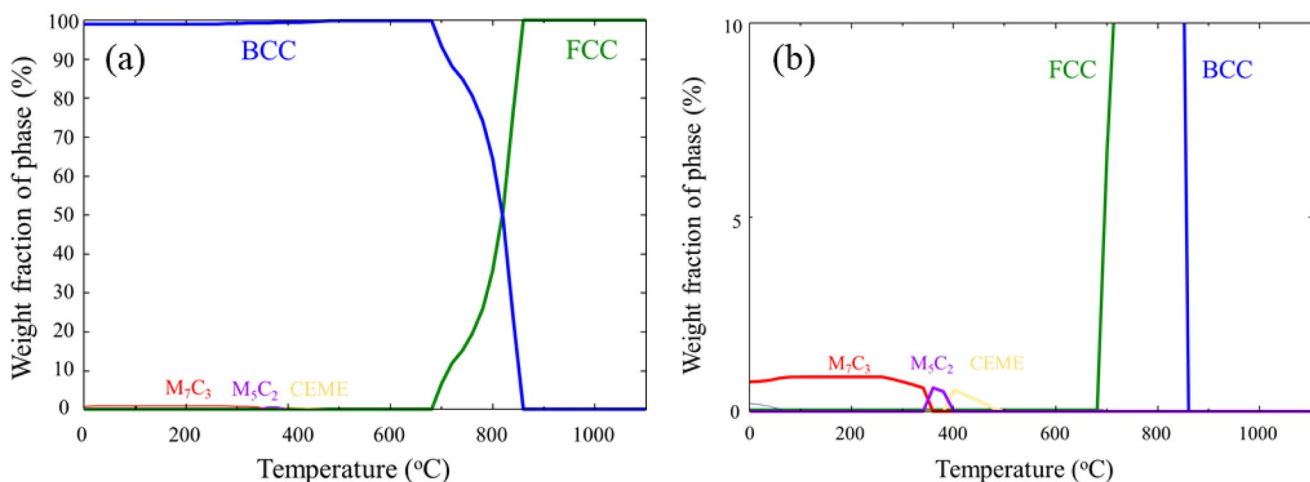


**Fig. 10** **a** Phase diagram of thermodynamic equilibrium and **b** partial enlarged phase diagram of PH

the dissolution of carbides in PH-600, resulting in the yield strength of PH-600 being lower than that of PH-200.

The dissolution of carbides can also be inferred from the cumulative probability of the nanohardness, as shown in Fig. 9e. The distribution of the nanohardness of PH-600 shifted to a lower value than those of PH-AS and PH-200. The decrease in precipitation hardening due to the dissolution of carbides in PH-600 appears to lead to reduced nanohardness in PH-600.

The variation in tensile strength among the PH specimens listed in Table 2 can be explained by the dissolution of carbides. In the case of PH-200, in which the volume fraction of the carbide phase may change slightly, the tensile strength remained similar to that of PH-AS. Conversely, in the case of PH-600, precipitation hardening decreased owing to carbide dissolution, leading to reduced tensile strength.

Microstructural analysis was performed to determine the microstructural changes that occurred during the heat treatment of the PH specimens. Figure 11 shows SEM images and SEM–EDS mapping images for carbon of the PH specimens. A noticeable decrease in the density and size of particles segregated near the grain boundaries is observed in PH-600 (Fig. 11e, f), compared to PH-AS (Fig. 11a, b) and PH-200 (Fig. 11c, d). SEM–EDS mapping images in Fig. 11b, d, f reveal that particles segregated at grain boundaries exhibit higher carbon content than the matrix, implying their carbide nature. In other words, these results clearly indicate carbide dissolution in PH-600, thereby influencing its mechanical properties.

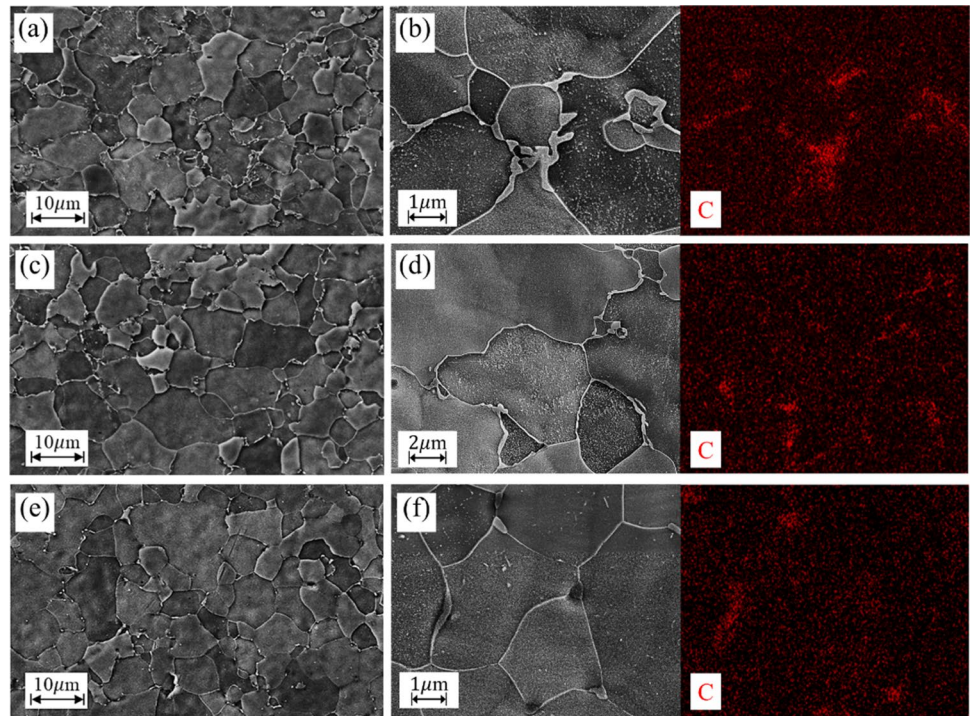
Furthermore, we analyzed the microstructural factors that caused differences in nanomechanical properties of  $\tau^*$  between PH specimens. Figure 12a shows a red load–displacement curve with a high  $\tau^*$  value and a blue load–displacement curve with a low  $\tau^*$  value obtained from PH-AS. SEM–EDS analysis was performed on the grain boundaries

near the indentations for the two load–displacement curves, and the results are shown in Fig. 12b, c. Figure 12b shows the SEM–EDS line-scanning data for carbon near the indentation where  $\tau^*$  was at a higher value. The carbon concentration increased near the grain boundaries, implying that carbon was segregated at the grain boundaries. Figure 12c shows SEM–EDS line-scanning data near the indentation where  $\tau^*$  was at a lower value. No concentration gradient of carbon solute was observed near the grain boundary. These results imply that carbon segregation at the grain boundary caused the difference in  $\tau^*$ .

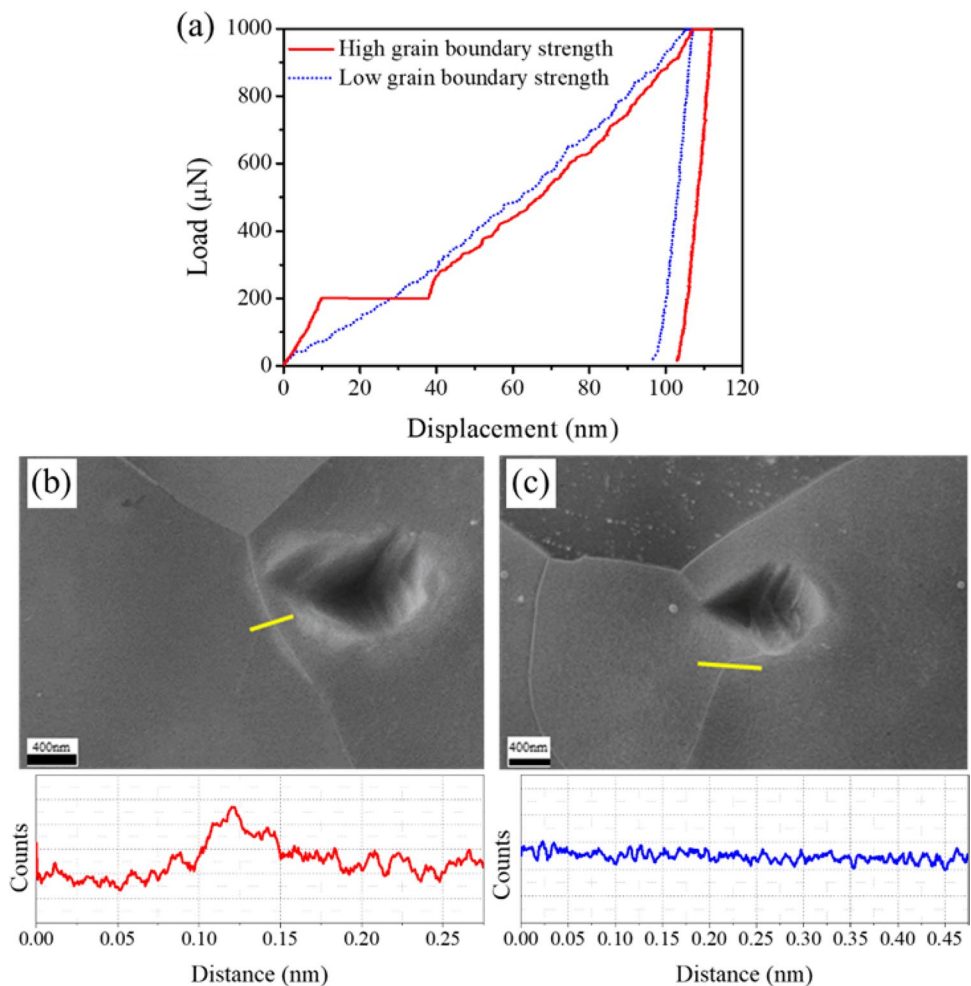
Based on the SEM (Fig. 11) and EDS (Fig. 12) results, the mechanical behavior of the PH specimens can be explained by microstructural factors. In the case of PH-200, the yield strength increased and the total elongation decreased compared to PH-AS, owing to the enhanced  $\tau^*$  induced by carbon segregation. The tensile strength of PH-200 remained similar to that of PH-AS because there was little change in the carbide volume fraction. For PH-600, carbide dissolution led to a decreased tensile strength of PH-600 compared to that of PH-AS and PH-200 and increased the concentration of carbon present as a solute in the matrix. Accordingly, a greater amount of carbon solute was segregated at the grain boundaries in PH-600 than in PH-AS and PH-200, resulting in the highest  $\tau^*$  for PH-600, as shown in Fig. 9. Consequently, although precipitation hardening decreased owing to carbide dissolution, the increase in Hall–Petch hardening resulting from carbon segregation at the grain boundary outweighed the reduction in precipitation hardening, ultimately leading to an increase in the yield strength of PH-600 compared to that of PH-AS. Additionally, the total elongation of PH-600 decreased compared with that of PH-AS owing to the enhanced  $\tau^*$  induced by carbon segregation.

The average  $\tau^*$  values for the IF-AS and PH specimens are presented in Fig. 13. In the PH specimens, grain boundary

**Fig. 11** **a** SEM image, **b** enlarged SEM image and corresponding SEM–EDS mapping image for carbon of PH-AS. **c** SEM image, **d** enlarged SEM image and corresponding SEM–EDS mapping image for carbon of PH-200. **e** SEM image, **f** enlarged SEM image and corresponding SEM–EDS mapping image for carbon of PH-600.



**Fig. 12** **a** load–displacement curves for nano-indentation tests, with the red solid line representing high grain boundary strength and the blue dotted line representing low grain boundary strength. **b** SEM–EDS line scanning data for carbon near the grain boundary corresponding to the red solid line in **a**. **c** SEM–EDS line scanning data for carbon near the grain boundary corresponding to the blue dotted line in **a** was obtained. Scanning line is indicated by yellow line in SEM images.



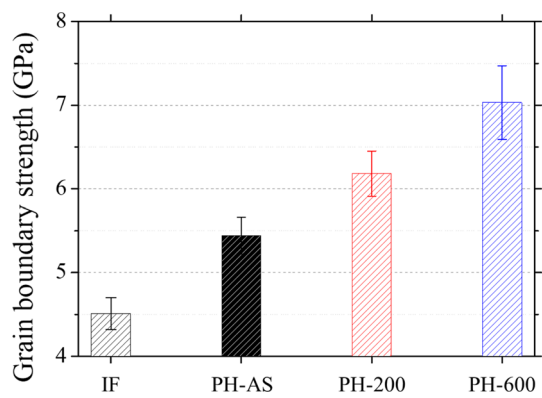


**Fig. 13** The average grain boundary strength of IF-AS and PH specimens

strengthening can be attributed to the carbon segregation at the grain boundary, which made the  $\tau^*$  value of the PH specimens much higher than that of IF-AS. Therefore, the occurrence of the yield-point phenomenon only in the PH specimens, contrary to IF-AS, as shown in Fig. 3, can be explained from the perspective of  $\tau^*$ , as presented in Fig. 1. Furthermore, it was confirmed that variations in  $\tau^*$  owing to changes in carbon distribution induced differences in the mechanical properties of the PH specimens. In summary,  $\tau^*$  is a critical microstructural factor that determines the yielding behavior and mechanical properties of PH specimens.

### 3.4 Grain Boundary Strengthening by Manganese Segregation

Although all the PH specimens exhibited a recrystallized microstructure, the numerous carbon solutes present in the material could interact with dislocations to potentially form a Cottrell atmosphere. Therefore, we investigated IF-2Mn steel fabricated by adding only manganese, a substitutional solute incapable of forming a Cottrell atmosphere, to IF steel. Figure 14 shows the microstructures of the heat-treated IF-2Mn specimens observed using SEM/EBSD. The average grain sizes of IF-2Mn-1 and IF-2Mn-2 were 42.2 and 49.9  $\mu\text{m}$ , respectively.

As shown in the uniaxial tensile test results of the IF-2Mn specimens in Fig. 15, the yield-point phenomenon was observed in all specimens, and the engineering stress–strain curves of each specimen differed. Although IF-2Mn-2 had a larger grain size of 49.9  $\mu\text{m}$  than IF-2Mn-1 with a grain size of 42.2  $\mu\text{m}$ , both specimens exhibited similar yield strength. This implies that there is a hardening mechanism that contributes to the yield strength of IF-2Mn-2 in addition to grain refinement hardening.

The load–displacement curves of IF-2Mn-1 (red) and IF-2Mn-2 (blue) are presented in Fig. 16a, b, respectively. The cumulative probability of  $\tau^*$  obtained from Fig. 16a, b is shown in Fig. 16c. The distribution of  $\tau^*$  shifted to its highest value in IF-2Mn-2 compared to that in IF-2Mn-1.

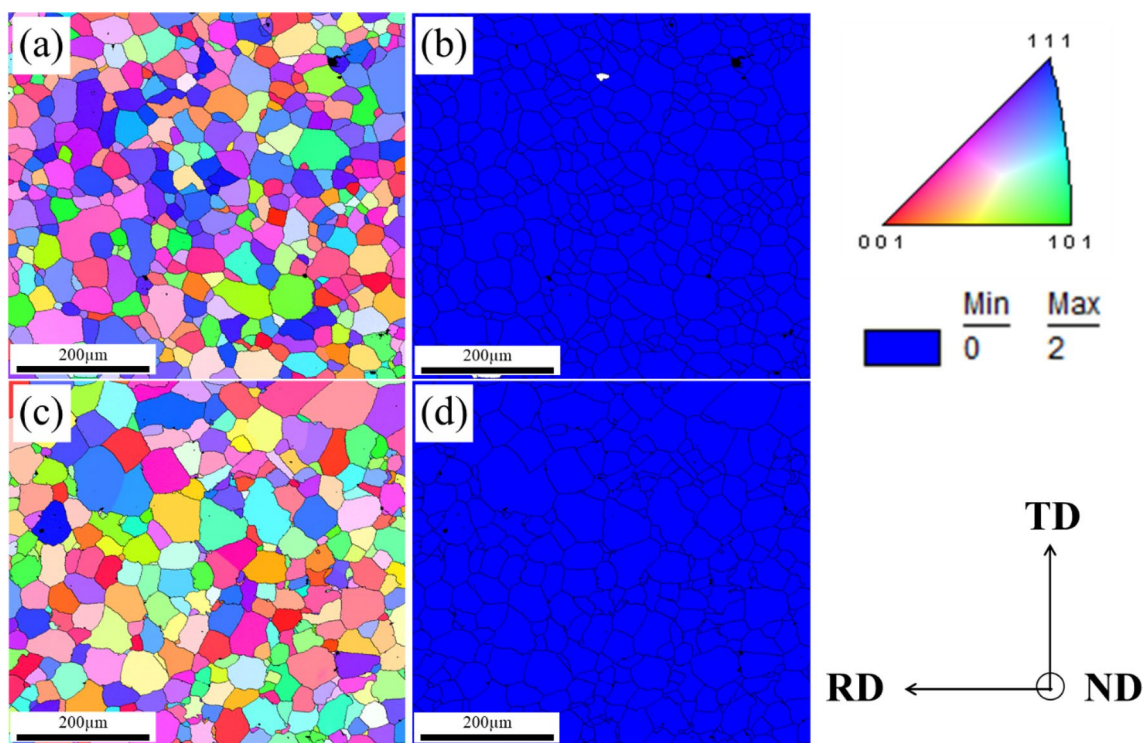


**Fig. 14** The EBSD maps of **a, b** IF-2Mn-1 and **c, d** IF-2Mn-2. **a, c** IPF ND map and **b, d** GOS map

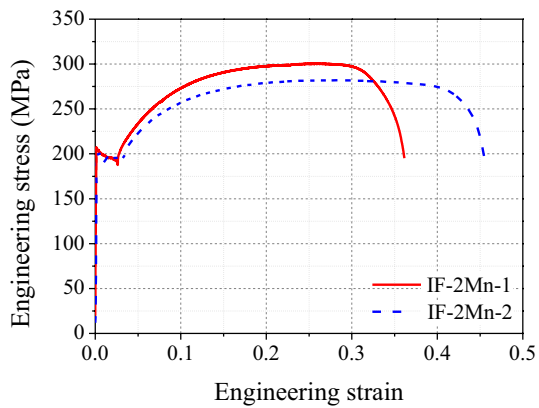


**Fig. 15** Engineering stress–strain curve of IF-2Mn specimens during uniaxial tensile test at 25 °C of room temperature for the strain rate  $10^{-3} \text{ s}^{-1}$

This result indicates that the yield strength of IF-2Mn-2 was similar to that of IF-2Mn-1, despite the larger grain size of IF-2Mn-2, demonstrating the increased Hall–Petch hardening due to the enhanced  $\tau^*$ .

EPMA was performed to investigate the microstructural factors that caused the grain boundary strengthening of IF-2Mn-2. Figure 17 shows the EPMA elemental maps for Mn, C, and Ti. Unlike IF-2Mn-1, distinct manganese segregation was observed near the grain boundaries in IF-2Mn-2. This result implies that the enhanced  $\tau^*$  induced by manganese segregation at the grain boundaries contributes to the increase in yield strength by enhancing the Hall–Petch hardening. Figure 18 shows the average  $\tau^*$  values for the IF-AS and IF-2Mn specimens. Compared to the IF-AS specimen, the IF-2Mn specimens exhibited a higher  $\tau^*$ . Despite the impossibility of the Cottrell atmosphere formation, the occurrence of the yield-point phenomenon in the IF-2Mn specimens, as shown in Fig. 15, can be attributed to the larger  $\tau^*$  in the IF-2Mn specimens compared to that in IF-AS, as explained by the mechanism shown in Fig. 1. These results, along with those from the PH specimens, offer

**Fig. 16** Load–displacement curve of **a** IF-2Mn-1 and **b** IF-2Mn-2. **c** Cumulative probability of grain boundary strength for IF-2Mn specimens

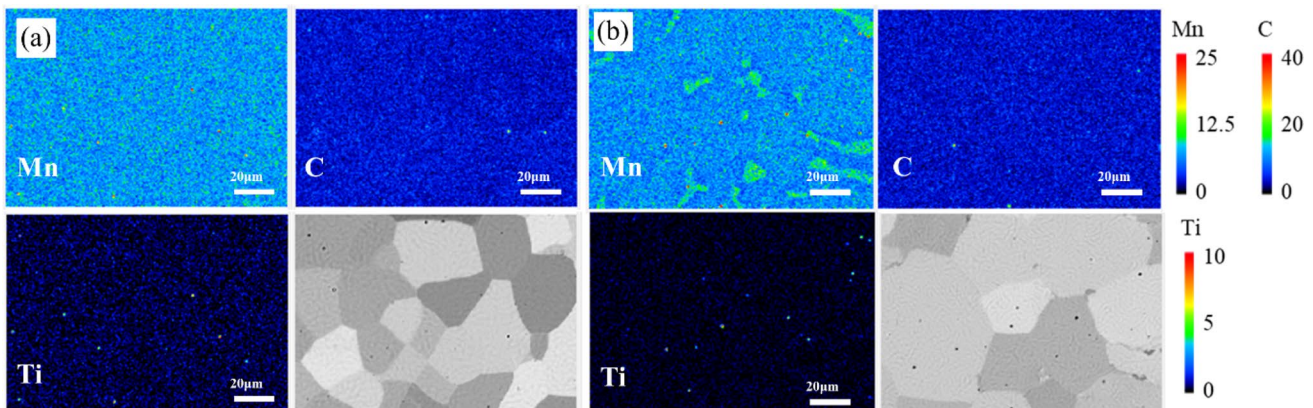
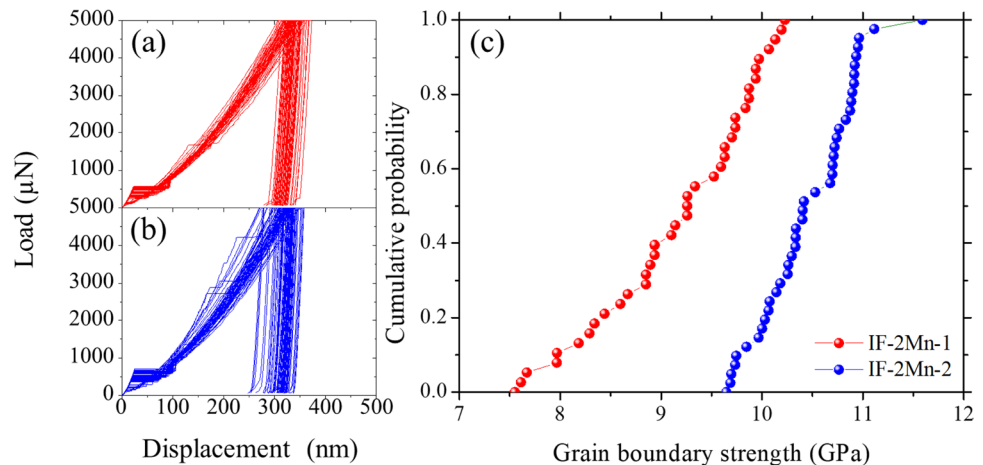


**Fig. 17** Electron Probe Micro Analyzer (EPMA) element maps of manganese, carbon and titanium for **a** IF-2Mn-1 and **b** IF-2Mn-2

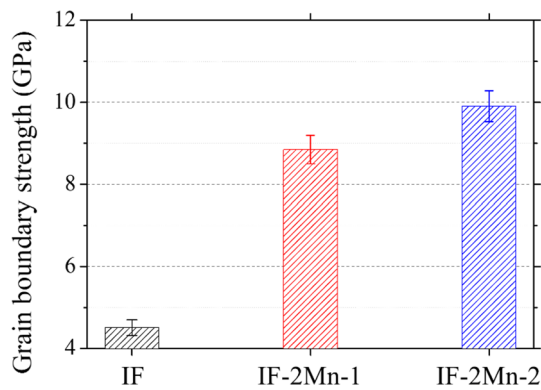


**Fig. 18** The average grain boundary strength of IF-AS and IF-2Mn specimens

further experimental evidence supporting the significant role of  $\tau^*$  in determining the yielding behavior and uniaxial tensile properties of recrystallized ferritic steels.

## 4 Conclusion

This study investigated the role of  $\tau^*$  in determining the yielding behavior and uniaxial tensile properties of recrystallized ferrite steels. Three ferritic steels with distinct chemical compositions (IF, PH, and IF-2Mn steel) were employed in this study. The main findings and conclusions are summarized as follows.

1. A methodology to estimate  $\tau^*$  using a nanoindentation test was proposed, and the reliability of this methodology was verified through Hall–Petch analysis and dislocation pile-up theory. Based on this methodology, the role of  $\tau^*$  in determining yielding behavior and mechanical properties was demonstrated.
2. Despite the PH specimens having similar grain sizes, the uniaxial tensile properties varied significantly among the different specimens owing to differences in the carbon distribution resulting from distinct heat treatment histories. The interplay between the reduction in precipitation hardening owing to carbide dissolution and the increase in  $\tau^*$  through carbon segregation at the grain boundaries played a crucial role in determining the uniaxial tensile properties of each specimen. In addition, the PH specimens exhibited a higher  $\tau^*$  than the IF-AS. This implies that the occurrence of the yield-point phenomenon in the PH specimens can be explained from the perspective of  $\tau^*$ .
3. In the IF-2Mn specimen, manganese segregation at the grain boundaries increased  $\tau^*$  and influenced the yield strength by enhancing the Hall–Petch hardening. Furthermore, despite the impossibility of Cottrell atmos-

phere formation, the yield-point phenomenon in the IF-2Mn specimens could be attributed to the larger  $\tau^*$  in the IF-2Mn specimens than that in IF-AS. These results, in conjunction with those of the PH specimens, provide additional experimental evidence underscoring the significant role of  $\tau^*$  in determining the yielding behavior and uniaxial tensile properties of recrystallized ferritic steels.

4. Our findings have significant implications for the design and optimization of ferritic steels. By controlling the grain boundary strength through solute segregation, the yielding behavior and tensile properties of steels can be tailored to meet specific engineering requirements. This study not only enriches the theoretical understanding of the microstructural mechanism for yielding behavior, but also guides the development of ferritic steels with the desired mechanical properties.

**Acknowledgements** This work was supported by the National Research Foundation of Korea (NRF) grants funded by the Ministry of Science and ICT (MSIT) (Grant Numbers 2019M3D1A1079215, 2021M3H4A6A01045764, 2021R1A2C3005096). The Institute of Engineering Research at Seoul National University provided research facilities for this work.

**Author contributions** B-SJ: Conceptualization, Methodology, Investigation, Writing–Original Draft. SL: Investigation. JY: Resources, Investigation. ESP: Resources, Methodology, HNH: Project administrations, Writing–Review and Editing, Funding acquisition.

**Funding** Open Access funding enabled and organized by Seoul National University.

## Declarations

**Conflict of interest** The authors declare that they have no known competing financial interests or personal relationships that could have appeared to influence the work reported in this paper.

**Open Access** This article is licensed under a Creative Commons Attribution 4.0 International License, which permits use, sharing, adaptation, distribution and reproduction in any medium or format, as long as you give appropriate credit to the original author(s) and the source, provide a link to the Creative Commons licence, and indicate if changes were made. The images or other third party material in this article are included in the article's Creative Commons licence, unless indicated otherwise in a credit line to the material. If material is not included in the article's Creative Commons licence and your intended use is not permitted by statutory regulation or exceeds the permitted use, you will need to obtain permission directly from the copyright holder. To view a copy of this licence, visit <http://creativecommons.org/licenses/by/4.0/>.

## References

1. S. Kondo, T. Mitsuma, N. Shibata, Y. Ikuhara, *Sci. Adv.* **2**, e1501926 (2016)

2. B. Liu, D. Raabe, P. Eisenlohr, F. Roters, A. Arsenlis, G. Hommes, *Acta Mater.* **59**, 7125–7134 (2011)
3. M.D. Sangid, T. Ezaz, H. Sehitoglu, I.M. Robertson, *Acta Mater.* **59**, 283–296 (2011)
4. H. Pan, Y. He, X. Zhang, *Materials* **14**, 1012 (2021)
5. J. Wang, *JOM* **67**, 1515–1525 (2015)
6. M. Rezayat, F. Najib, *Met. Mater. Int.* **29**, 235–246 (2023)
7. C.-L. Chen, R. Sutrisna, *Met. Mater. Int.* **29**, 1739–1749 (2023)
8. R. Schouwenaars, M. Seefeldt, P. Van Houtte, *Acta Mater.* **58**, 4344–4353 (2010)
9. N.H. Heo, Y.-U. Heo, S.K. Kwon, N.J. Kim, S.-J. Kim, H.-C. Lee, *Met. Mater. Int.* **24**, 265–281 (2018)
10. J.P. Hirth, J. Lothe, T. Mura, *J. Appl. Mech.* **50**, 476–477 (1983)
11. D. An, X. Liu, Y. Liu, X. Li, J. Chen, *Mater. Charact.* **195**, 112545 (2023)
12. T. Tsuchiyama, S. Araki, S. Takaki, *J. Iron Steel Inst. Jpn.* **106**, 382–390 (2020)
13. Z. Huang, C. Yang, L. Qi, J.E. Allison, A. Misra, *Mater. Sci. Eng. A* **742**, 278–286 (2019)
14. Z. Li, J. Zhang, Y. Zhai, J. Zhang, X. Wang, Z. Zhang, S. Mao, X. Han, *Mater. Res. Lett.* **10**, 539–546 (2022)
15. F. Pettinari-Sturmelt, G. Saada, J. Douin, A. Coujou, N. Clément, *Mater. Sci. Eng. A* **387**, 109–114 (2004)
16. N. Petch, *J. Iron Steel Inst.* **174**, 25–28 (1953)
17. E. Hall, *Proc. Phys. Soc. Sec. B* **64**, 747 (1951)
18. S. Takaki, D. Akama, N. Nakada, T. Tsuchiyama, *Mater. Trans.* **55**, 28–34 (2014)
19. M.-Y. Seok, I.-C. Choi, J. Moon, S. Kim, U. Ramamurty, J.-I. Jang, *Scr. Mater.* **87**, 49–52 (2014)
20. N. Hansen, *Mater. Sci. Eng. A* **409**, 39–45 (2005)
21. J. Lee, H. Kim, K. Jeong, S.-J. Park, J. Moon, S.-G. Kang, H.N. Han, *J. Mater. Res. Technol.* **14**, 2897–2908 (2021)
22. J.P. Hirth, *The Influence of Grain Boundaries on Mechanical Properties* (Springer, 1972)
23. F. Jiang, T. Masumura, T. Tsuchiyama, S. Takaki, *ISIJ Int.* **59**, 1929–1931 (2019)
24. K. Takeda, N. Nakada, T. Tsuchiyama, S. Takaki, *ISIJ Int.* **48**, 1122–1125 (2008)
25. S. Araki, K. Fujii, D. Akama, T. Tsuchiyama, S. Takaki, T. Ohmura, J. Takahashi, *ISIJ Int.* **58**, 1920–1926 (2018)
26. N. Nakada, M. Fujihara, T. Tsuchiyama, S. Takaki, *ISIJ Int.* **51**, 1169–1173 (2011)
27. S. Gao, A. Shibata, M. Chen, N. Park, N. Tsuji, *Mater. Trans.* **55**, 69–72 (2014)
28. A.H. Cottrell, B.A. Bilby, *Proc. Phys. Soc. Sec. A* **62**, 49 (1949)
29. T. Yokobori, *Phys. Rev.* **88**, 1423 (1952)
30. D. Wilson, B. Russell, *Acta Metall.* **8**, 36–45 (1960)
31. D. Wilson, B. Russell, *Acta Metall.* **8**, 468–479 (1960)
32. W.G. Johnston, J.J. Gilman, *J. Appl. Phys.* **30**, 129–144 (1959)
33. G.T. Hahn, *Acta Metall.* **10**, 727–738 (1962)
34. M. Liu, Y. Liu, H. Li, *Mater. Charact.* **205**, 113369 (2023)
35. M. Chen, W. Deng, M. Wang, J. Li, S. Xing, *Mater. Sci. Eng. A* **875**, 145095 (2023)
36. B.-S. Jeong, K. Lee, S. Park, W. Cho, L. Park, H.N. Han, *Mater. Trans.* **63**, 1296–1303 (2022)
37. Y. Tian, S. Gao, L. Zhao, S. Lu, R. Pippin, Z. Zhang, N. Tsuji, *Scr. Mater.* **142**, 88–91 (2018)
38. S. Gao, M. Chen, S. Chen, N. Kamikawa, A. Shibata, N. Tsuji, *Mater. Trans.* **55**, 73–77 (2014)
39. G. Pharr, W. Oliver, *MRS Bull.* **17**, 28–33 (1992)
40. K.L. Johnson, *Contact Mechanics* (Cambridge University Press, Cambridge, 1987)
41. D. Lorenz, A. Zeckzer, U. Hilpert, P. Grau, H. Johansen, H. Leipner, *Phys. Rev. B* **67**, 172101 (2003)
42. C.A. Schuh, *Mater. Today* **9**, 32–40 (2006)
43. A. Zbib, D.F. Bahr, *Metall. Mater. Trans. A* **38**, 2249–2255 (2007)
44. T.-H. Ahn, C.-S. Oh, K. Lee, E.P. George, H.N. Han, *J. Mater. Sci. Res.* **27**, 39–44 (2012)
45. T.-H. Ahn, S.B. Lee, K.-T. Park, K.H. Oh, H.N. Han, *Mater. Sci. Eng. A* **598**, 56–61 (2014)
46. Y. Kim, T.-H. Ahn, D.-W. Suh, H.N. Han, *Scr. Mater.* **104**, 13–16 (2015)
47. W. Cho, B.-S. Jeong, E. Shin, S. Park, J. Jung, H. Na, S.-I. Kim, H.N. Han, *Mater. Sci. Eng. A* **856**, 144004 (2022)
48. R.W.K. Honeycombe, *The Plastic Deformation of Metals* (Edward Arnold, Maidenhead, 1968)
49. A. Smith, H. Luo, D.N. Hanlon, J. Sietsma, S. van der Zwaag, *ISIJ Int.* **44**, 1188–1194 (2004)

**Publisher's Note** Springer Nature remains neutral with regard to jurisdictional claims in published maps and institutional affiliations.